

Locality Error Free Effective Core Potentials for 3d Transition Metal Elements Developed for the Diffusion Monte Carlo Method*

Tom Ichibha ^{a,1,2,†} Yutaka Nikaido ^{a,1} M. Chandler Bennett,² Jaron T. Krogel,² Kenta Hongo,³ Ryo Maezono,¹ and Fernando A. Reboredo^{2,‡}

¹*School of Information Science, JAIST, Asahidai 1-1, Nomi, Ishikawa 923-1292, Japan*

²*Materials Science and Technology Division, Oak Ridge National Laboratory, Oak Ridge, Tennessee 37831, USA*

³*Research Center for Advanced Computing Infrastructure, JAIST, Asahidai 1-1, Nomi, Ishikawa 923-1292, Japan*

(Dated: October 13, 2023)

Pseudopotential locality errors have hampered the applications of the diffusion Monte Carlo (DMC) method in materials containing transition metals, in particular oxides. We have developed locality error free effective core potentials, pseudo-Hamiltonians, for transition metals ranging from Cr to Zn. We have modified a procedure published by some of us in [M.C. Bennett et al, JCTC **18** (2022)]. We carefully optimized our pseudo-Hamiltonians and achieved transferability errors comparable to the best semilocal pseudopotentials used with DMC but without incurring in locality errors. Our pseudo-Hamiltonian set (named OPH23) bears the potential to significantly improve the accuracy of many-body-first-principles calculations in fundamental science research of complex materials involving transition metals.

^a These two authors made the equivalent contributions.

I. INTRODUCTION

While initially *ab initio* simulations were primarily used to provide physical insights on properties that are difficult to be observed experimentally [1], or to verify and understand experimental data[2], nowadays, they are increasingly being used to find new stable crystal structures [1, 3]. This research aims to predict, before experiments, novel materials that have targeted physical properties. The importance of *ab initio* simulations is therefore increasing in materials science. But the demand to predict a new stable material is also increasing the accuracy required in the results; which in turns demands improving the underlying theory.

The diffusion Monte Carlo (DMC) method is emerging as one the most practical many-body *ab initio* methods, because of its moderate cost scaling per step ($\sim N^3$) and excellent parallelizability [4, 5]. In addition, DMC has comparable accuracy and reliability to the coupled cluster single-double and perturbative triple [CCSD(T)] method [6–8]. DMC is often implemented within the fixed-node (or fixed-phase) approximation (FNDMC) to avoid the fermion sign problem [4, 9, 10]. In FNDMC the nodes (phase) of the ground state wavefunction Ψ_0 are fixed by the ones given by trial

wave function Ψ_T provided by a different *ab initio* method, like Kohn-Sham density functional theory (DFT) [11]. The fixed-node (phase) approximation introduced a positive bias in the total energy known as “nodal errors”. Nodal errors can be systematically reduced using multideterminant expansions, [12, 13] orbital optimization methods, or back-flow approximations [14–16].

Accurate effective core potentials (ECPs) are also needed for practical problems. ECPs are constructed so as they accurately reproduce multiple electronic scattering properties of all-electron (AE) calculations, often obtained at the frozen core approximation level. In DMC the core electrons and ionic cores are replaced by an ECP to mitigate the computational cost. Without ECPs, the calculation cost of FNDMC scales as $Z^{5.5-6.5}$, where Z is the nuclear charge [17, 18]. With ECPs, the cost scaling gets reduced to be $Z_{\text{ECP}}^{3.4}$, where Z_{ECP} is the effective core charge [19].

The ECP approximation, however, brings a bias depending on the quality of ECPs (ECP errors) for any *ab initio* method [20]. The typical semilocal form of ECP shown in Eq. (4) makes another type of errors (locality errors) when evaluated in FNDMC. Locality errors stem from the projection operators to the angular momentum channels: $\sum_{m=-\ell}^{\ell} |\ell m\rangle \langle \ell m|$. Here, $|\ell m\rangle$ is the eigenstate for angular momentum (ℓ, m) . Some approximation is needed to estimate the projections, $\sum_{m=-\ell}^{\ell} \Psi_T |\ell m\rangle \langle \ell m| \Psi_0$, avoiding an additional sign problem [21]. The conventional locality approximation [21] and the alternative T -moves [22, 23] approximation can introduce errors in the range of 0.2–0.3 eV per atom for the 3d transition metal elements for cohesive energies and relevant properties [24–26]. The size of this error is roughly 10 times larger than the remaining ECP’s errors. The state-of-the-art ECPs for DMC reach 0.02–0.03 eV errors for the binding curves of 3d transition metal and oxygen dimers in CCSD(T) calculations [27, 28]. Therefore, the locality errors currently constitute the main contribution of ECP errors in DMC applications to 3d transition metal composites.

* Notice: This manuscript has been authored by UT-Battelle, LLC, under contract DE-AC05-00OR22725 with the US Department of Energy (DOE). The US government retains and the publisher, by accepting the article for publication, acknowledges that the US government retains a nonexclusive, paid-up, irrevocable, worldwide license to publish or reproduce the published form of this manuscript, or allow others to do so, for US government purposes. DOE will provide public access to these results of federally sponsored research in accordance with the DOE Public Access Plan (<http://energy.gov/downloads/doe-public-access-plan>).

[†] ichibha@icloud.com
[‡] reboredofa@ornl.gov

Moreover, these locality errors are sometimes larger for the $4d$ transition metal elements [29]. The magnitude of locality errors is dependent on the quality of the trial wavefunction Ψ_T , including the Jastrow factor [30, 31]. Therefore, any comparison of results of different FNDMC calculations (required to predict magnetic properties, defect formation energies, band gaps etc.) becomes more dependent on the trial wave functions. Often trial wave functions have different locality errors since they are optimized [32] independently. The uncertainty of the cancellation of locality errors increases with the size of the electronic system considered. Accordingly, similar to the case of nodal errors, avoiding locality errors is a priority to improve the overall accuracy of the FNDMC approach.

Another alternative, the auxiliary field quantum Monte Carlo (AFQMC) approach, [33–36] can avoid using pseudopotentials altogether with a frozen core approximation. Moreover, pseudopotentials can be incorporated in AFQMC without incurring in locality errors. AFQMC calculations are often one or two orders of magnitude more expensive than FNDMC. Therefore, alternative ways to accurately represent atomic cores, that do not include locality errors or increase significantly the computational cost, must be developed in FNDMC to compete in accuracy with AFQMC.

A possible approach to avoid the locality errors in FNDMC is the pseudo-Hamiltonian (PH) framework [37]. Although the PH framework was originally proposed in 1989 [37], this framework has been investigated only in a few cases [38–40]. This is due to the numerical difficulty to satisfy the constraint that the eigenenergies of nodeless orbitals increasing monotonically with the angular momentum ℓ [38]. It is even harder to correctly describe the scattering properties of multiple angular-momentum channels together along with the constraint [38]. This constraint makes it difficult to construct an accurate PH, especially for some first row elements and Ar-core $3d$ TMs [41].

However, the PH framework should be now reconsidered because recent progresses such as the multideterminant expansion [12, 13] and Pfaffian pairing wave function [42–44], and increased computational resources have made possible to reduce nodal and statistical errors in FNDMC so much that locality errors may become the leading source of error in delicate energy sensitive comparisons involving transition metals. Therefore, some of us have developed a theoretical framework and procedures to construct PHs [24, 45] and demonstrated their effectiveness for the Co element [45].

In this paper, we report newly constructed PH's for the $3d$ transition metal elements from Cr to Zn with a slight modification of a previous procedure [45]. We also compare the transferability of our PHs with highly accurate semilocal pseudopotentials used with FNDMC [27, 28, 46–49].

The rest of the paper is organized as follows. In section II, we explain the theory and the procedures used to generate multiple PHs using a combination of Hartree-Fock (HF) and CCSD(T) methods for each transition metal (TM) element. In Section III, we explain the details of calculations conducted for the optimization and verification of the PHs. In Subsection

IV A, we explain how we selected the optimal PHs (named OPH23) based on the atomic properties and TM-O binding curves from the multiple candidate PHs we constructed for each TM element. In Subsection IV B, we confirmed the reproducibility of AE binding curves of TM–O and TM–F molecules by the OPH23 set, which is compared with highly accurate semilocal pseudopotentials used with FNDMC, BFD [46, 47], SBKJC [48, 49], and ccECP [27, 28]. Finally, we summarize our study in Section V.

II. THEORY

The general form of pseudo-Hamiltonian [37] in spherical symmetry is given by:

$$\hat{h}^{\text{PH}}(r) = \frac{1}{2} \hat{p} [1 + a(r)] \hat{p} + v_{\text{local}}^{\text{PH}}(r) + v_{L^2}(r) \hat{L}^2. \quad (1)$$

Here, \hat{p} is the momentum operator. The eigenenergies of nodeless orbitals necessarily monotonically increase with the angular momentum ℓ [37]. We choose to fix the radial mass to be constant, $a(r) = 1$, as in the previous work by some of the authors [41]. Then, the first term on the right hand side of Eq. (1) comes down to the usual kinetic energy operator:

$$\frac{\hat{p} [1 + a(r)] \hat{p}}{2} \rightarrow \frac{\hat{p}^2}{2}. \quad (2)$$

This constraint is not required in theory but needed to be able to use general *ab initio* packages with PHs because the variable radial mass is not currently implemented in most codes used to obtain the trial functions for FNDMC. However, a sufficient transferability was achieved with this choice in the case of cobalt [41].

Our PH is defined as

$$\begin{aligned} \hat{v}^{\text{PH}}(r) &= v_{\text{local}}^{\text{PH}}(r) + v_{L^2}(r) \hat{L}^2 \\ &= v_{\text{local}}^{\text{PH}}(r) + v_{L^2}(r) \sum_{\ell=0}^{\infty} \sum_{m=-\ell}^{\ell} \ell(\ell+1) |\ell m\rangle \langle \ell m|. \end{aligned} \quad (3)$$

The $|\ell m\rangle$ are the scalar spherical harmonics as defined in Appendix A. This PH with the constant radial mass looks similar to the semilocal pseudopotentials

$$\hat{v}^{\text{SL}}(r) = v_{\text{local}}^{\text{SL}}(r) + \sum_{\ell=0}^{M-1} \sum_{m=-\ell}^{\ell} v_{\ell}(r) |\ell m\rangle \langle \ell m|. \quad (4)$$

Here, $M - 1$ is the maximum angular momentum channel of the core orbitals; $M=2$ for the neon core pseudopotentials for $3d$ transition metal elements.

A. Initial values for the PHs

Our strategy for PHs construction is to construct the parameter functions of the PH, $\hat{v}_{\text{local}}^{\text{PH}}(r)$ and $v_{L^2}(r)$, using the parameter functions of a successful semilocal pseudopotential

as starting point. For 3d transition metal elements, we construct the starting $\hat{v}_{\text{local}}^{\text{PH}}(r)$ and $v_{L^2}(r)$ so as they reproduce the pseudopotential up to the d channel:

$$\begin{aligned} \langle \ell m | \hat{v}^{\text{PH}} | \ell m \rangle &= \langle \ell m | \hat{v}^{\text{SL}} | \ell m \rangle, \\ (\ell = 0, 1, 2; m = -\ell, -\ell + 1, \dots, +\ell). \end{aligned} \quad (5)$$

Both sides in Eq. (5) are invariant with respect to m as is clear from Eqs. (3) and (4). Thus, there are actually three unique equations:

$$v_{\text{local}}^{\text{PH}}(r) = v_{\text{local}}^{\text{SL}}(r) + v_0(r), \quad (6)$$

$$v_{\text{local}}^{\text{PH}}(r) + 2v_{L^2}(r) = v_{\text{local}}^{\text{SL}}(r) + v_1(r), \quad (7)$$

$$v_{\text{local}}^{\text{PH}}(r) + 6v_{L^2}(r) = v_{\text{local}}^{\text{SL}}(r). \quad (8)$$

Equations (6)–(8) can be solved imposing a condition of linear dependence:

$$2v_0(r) - 3v_1(r) = 0. \quad (9)$$

To facilitate the optimization, we choose to modify $v_1(r)$ as the function of $v_0(r)$

$$v_1[v_0(r)] = (2/3)v_0(r), \quad (10)$$

because the semilocal $3p$ orbitals are for transition metals much less important than the valence $3d$ and $4s$ orbitals to describe chemical reactions [27, 50]. As a result, the starting parameter functions of PH are given from Eqs. (6)–(8) and Eq. (10) as

$$v_{\text{local}}^{\text{PH}} = v_{\text{local}}^{\text{SL}} + v_0, \quad v_{L^2} = -(1/6)v_0. \quad (11)$$

In addition, the parameter function v_{L^2} has to satisfy the following bounding condition [24, 41]:

$$1 + 2r^2 v_{L^2}(r) > 0. \quad (12)$$

The left-hand side in Eq. (12) corresponds to the value of an effective mass multiplying the electron angular momentum. A negative effective mass would lead to an electronic wavefunction to localize into a delta function lowering its energy. Accordingly, Eq. (12) must be satisfied to avoid unphysical results. Therefore, we replace $v_{L^2}(r)$ with a smooth and shifted ramp function $v'_{L^2}(r)$ that satisfies the bounding condition:

$$2r^2 v_{L^2}(r) \rightarrow 2r^2 v'_{L^2}(r) \equiv \mathcal{R}_S(2r^2 v_{L^2}(r), \delta b, \delta b_s). \quad (13)$$

The ramp function $\mathcal{R}_S(x)$ is shown in Figure 1. When $x = 2r^2 v_{L^2}(r)$ approaches the lower bound -1 from the positive side, $\mathcal{R}_S(x)$ smoothly converges to $-1 + \delta b_s$; $2r^2 v'_{L^2}(r)$ always satisfy the condition (12). When $x = 2r^2 v_{L^2}(r)$ becomes much larger than the lower limit -1 , $\mathcal{R}_S(x)$ smoothly converges to $x = 2r^2 v_{L^2}(r)$. δb decides the width of connection region between the constant and proportional regions in \mathcal{R}_S . The mathematical details of \mathcal{R}_S can be found in previous works [24, 41].

The difference between $2r^2 v_{L^2}(r)$ and $2r^2 v'_{L^2}(r)$:

$$\Delta(r) \equiv 2v'_{L^2}(r) - 2v_{L^2}(r) \quad (14)$$

was found to be well fitted by Gaussian functions in the case of cobalt [41]: $\Delta(r)$ with $\mathcal{R}_S(2r^2 v_{L^2}(r), \delta b = 1.6 \text{ Ha}, \delta b_s = 5 \times 10^{-4} \text{ Ha})$ was expanded by three Gaussian primitives with exponent values being 12.5, 18.75, and 28.128 Bohr⁻²[41]. In this work, we also expand $\Delta(r)$ in the same manner for the 3d transition elements. Eventually, we replace $2r^2 v_{L^2}(r)$ as

$$2r^2 v_{L^2}(r) \rightarrow 2r^2 v''_{L^2}(r) \equiv 2r^2 v_{L^2}(r) + r^2 \Delta_{\text{expanded}}(r). \quad (15)$$

From these initial values, the coefficients and coordinates of the Gaussian functions are optimized along with $\hat{v}_{\text{local}}^{\text{PH}}$ and v_{L^2} .

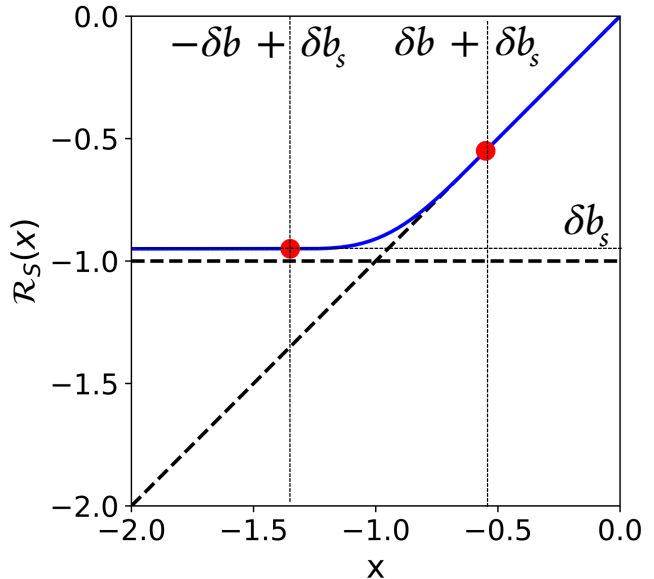


FIG. 1. Plot of the smooth and shifted ramp function. This figure is a reprint of Fig. 8 of our previous work [24] with small modification.

B. Pseudo-Hamiltonian construction

We choose the BFD semilocal pseudopotentials to define the initial parameter functions of our PHs via Eqs. (6)–(8) because of their simple parameterization. The core size of our PHs is the neon core as well as BFD, SBKJC, and ccECP. Ne-core pseudopotentials have been found to have better transferability than Ar-core in general with FNDMC method [50–52].

We optimize the parameters in \hat{v}^{PH} via three steps. In the first step, we conduct optimization to reproduce all the valence orbital norms and eigenenergies as well as neutral excitation and ionization energy spectrum in $4s$ and $3d$ levels obtained with the HF method with SBKJC pseudopotential. In the second step, we select the PH that best reproduces the TM–O binding curve among the multiple PHs for each element. In the third step, we further optimize the selected PHs so as to reproduce all the valence orbital norms and eigenenergies at the HF level and energy spectrum at the CCSD(T) level with

ccECP pseudopotential. The details of objective functions and procedures are described in the following subsections.

1. Hartree-Fock optimization

TABLE I. Reference electronic states for optimizing the PH of each element.

Cr	Mn	Fe	Co	Ni	Cu	Zn
$4s^1 3d^5$	$4s^2 3d^5$	$4s^2 3d^6$	$4s^2 3d^7$	$4s^1 3d^9$	$4s^1 3d^{10}$	$4s^2 3d^{10}$

The reference electronic states used to optimize the PHs in HF are listed in Table I. In general, we select the atomic ground state as the reference state. However, for the nickel case, because we could not obtain a solution that satisfies the bounding condition in Eq. (12) with the ground state $4s^2 3d^8$, we select the nearly degenerated state $4s^1 3d^9$ as the reference state.

For each element, we optimize the pseudo-Hamiltonian to minimize the following cost function:

$$\mathcal{O}^{\text{HF}} = \omega_1 \mathcal{O}_{\text{Eigenvalue}} + \omega_2 \mathcal{O}_{\text{Norm}} + \omega_3 \mathcal{O}_{\text{Bound}} + \omega_4 \mathcal{O}_{\text{Excitation}}^{\text{HF,SBKJC}}, \quad (16)$$

where,

$$\mathcal{O}_{\text{Eigenvalue}} = \sum_i \left[\left(\varepsilon_i^{\text{PH}} - \varepsilon_i^{\text{SBKJC}} \right) / \varepsilon_i^{\text{SBKJC}} \right]^2, \quad (17)$$

$$\mathcal{O}_{\text{Norm}} = \sum_i \left[\langle \phi_i^{\text{PH}} | \phi_i^{\text{PH}} \rangle_{r>0.8a_0} - \langle \phi_i^{\text{SBKJC}} | \phi_i^{\text{SBKJC}} \rangle_{r>0.8a_0} \right]^2, \quad (18)$$

$$\mathcal{O}_{\text{Bound}} = \int dr \left[\mathcal{R}_S \left(2r^2 v''_{L^2}(r), \delta b', \delta b'_s \right) - 2r^2 v''_{L^2}(r) \right], \quad (19)$$

$$\mathcal{O}_{\text{Excitation}}^{\text{HF,SBKJC}} = \sum_{j \ni (3d, 4s)} \left[\frac{\Delta E_j^{\text{HF,PH}} - \Delta E_j^{\text{HF,SBKJC}}}{\Delta E_j^{\text{HF,SBKJC}}} \right]^2. \quad (20)$$

\sum_i indicates a summation over all the valence orbitals. $\sum_{j \ni (3d, 4s)}$ indicates a summation over excited and ionized electronic states in $3d$ and $4s$ levels. Further explanation is found in the last paragraph of this subsection. $\langle \rangle_{r>0.8a_0}$ indicates an integral outside of the $0.8 a_0$ (a_0 : Bohr radius) radius sphere around the core center. $\mathcal{O}_{\text{Eigenvalue}}$ is lower when the orbital eigenenergies are reproduced better. $\mathcal{O}_{\text{Norm}}$ is lower when the integration of each orbital norm outside of the $0.8 a_0$ cutoff is reproduced better.

The starting PH used for subsequent optimization initially alters the shape of the p-channel found in the reference ECP (see Eq. (10)). During PH optimization, the quality of the p-channel is restored—in balance with the others—since $3p$ orbitals are included in the cost function in Eqs. (17) and (18). In $3d$ transition metals, the $3p$ orbitals are highly localized, deep and inert. Enforcing the norm and eigenvalues for the

$3p$ subshell has been shown to be sufficient to obtain accurate pseudopotentials for $3d$ transition metals. [53].

$\mathcal{O}_{\text{Bound}}$ is larger when the bounding condition (12) approaches being violated, and is otherwise almost zero. We employ $\delta b' = 0.25$ Ha and $\delta b'_s = 5 \times 10^{-3}$ Ha as our previous work [41].

$\mathcal{O}_{\text{Excitation}}^{\text{HF,SBKJC}}$ is lower when the energy spectrum of neutral excitation and ionization in the $3d$ and $4s$ levels are reproduced better.

The electron transitions in $3d$ and $4s$ orbitals and a variety of oxidation states are essential for the chemistry of $3d$ transition metals [27, 50]; thus they are included in Eq.(20). However, following a proven procedure in the literature for TM pseudo potentials[53], we do not consider the $3p$ to $4p$ levels excitation in the energy spectrum in Eq. (20).

Additionally, it is known that TM-O dimers strongly hybridize s,p,d orbitals. Therefore, since excitations to $4p$ are not weighted in Eq. (20), we performed additional test calculations of TM-O dimer binding curves to assess the transferability of our PHs (See II B 2).

There are still some degrees of freedom to choose: which excited and ionized states are considered in the evaluation of Eq. (20). We take into account every possible combination of $3d$ and $4s$ electrons from the charge neutral to $+X$ charged states, where the electron configuration is decided by the Hund's rules. We sometimes ignore a small number of excited states which cannot be calculated (when either the HF or CCSD(T) calculations do not converge). We optimize a PH for every $X=2-6$. We denote them in the following sections as HFOPT(X), respectively.

2. Binding Curve Selection

For each TM, we select a HFOPT(X) that best reproduces the molecular TM–O binding curve given by CCSD(T) in order to further optimize it at the third step.

3. Many-body correction

We make minor and major modifications to the cost function in Eq. (16) and further optimize the selected PH to minimize the modified cost function. The minor modification is using the ccECP pseudopotentials [27, 28] instead of the SBKJC pseudopotentials to provide the reference HF results; we found that ccECP pseudopotentials tend to reproduce slightly better the AE CCSD(T) TM–O binding curves. The major modification we made is to replace $\mathcal{O}_{\text{Excitation}}^{\text{HF,SBKJC}}$ in Eq. (20) with

$$\mathcal{O}_{\text{Excitation}}^{\text{CCSD(T),ccECP}} = \sum_{j \ni (3d, 4s)} \left(\frac{\Delta E_j^{\text{HF,CCOPT}} - \Delta E_j^{\text{CC}}}{\Delta E_j^{\text{CC}}} \right)^2, \quad (21)$$

$$\Delta E_j^{\text{CC}} \equiv \Delta E_j^{\text{HF,HFOPT}} - \Delta E_j^{\text{CCSD(T),HFOPT}} + \Delta E_j^{\text{CCSD(T),ccECP}} \quad (22)$$

[45]. Here, HFOPT is the PH that we select at the second step. CCOPT is the PH we optimize at this third step. The minimization of cost function in Eq. (21) corresponds to the optimization so as to reproduce the electron excitation energies at the CCSD(T) level (see Appendix B). The advantage of Eq. (21) is not including $\Delta E_i^{\text{CCSD(T),CCOPT}}$, which requires expensive CCSD(T) calculations for hundreds of parameter updates.

We compare the best HFOPT and CCOPT in terms of reproducibility of AE TM–O binding curve and AE atomic ionization energies. We name the better PH OPH23, the optimal pseudoHamiltonian produced in 2023. We compare the OPH23’s reproducibility of AE TM–O and AE TM–F binding curves with highly accurate semilocal pseudopotentials used with FNDMC, BFD[46, 47], SBKJC[48, 49], and ccECP[27, 28] in Section IV.

III. CALCULATION DETAILS

We used libraries in the Nexus workflow management software[54] to optimize the PHs and convert ECP file format. We employed the Nelder–Mead algorithm[55, 56] implemented in SciPy[57] for parameter fitting of PHs. During the optimization process, we used a numerical atomic Hartree–Fock code [58, 59] to evaluate the eigenenergies, norms, and excitation energies of atoms. We used the Molpro code[60, 61] to evaluate the ΔE_j^{CC} term of Eq. (22) and the dimer binding curves and atomic excitation energies with CCSD(T). We evaluated the dimer binding curves with our PHs and semilocal pseudopotentials used with FNDMC: BFD[46, 47], SBKJC[48, 49], and ccECP[27, 28], for comparison, and by AE calculations as the reference. Here, we truncated the $\ell > 7$ terms of PHs in Eq. (3) because Molpro cannot deal with \hat{L}^2 directly. We have confirmed that the binding curve sufficiently converges with this truncation in the case of Co–O. We used the 10th order Douglas–Kroll–Hess relativistic Hamiltonian[62, 63] for the AE calculations. We used the non-relativistic Hamiltonian for calculations with ECPs.

We evaluated the ionization energies shown in Figures 2 and 3 with the complete basis set (CBS) limit calculated with the fully uncontracted aug-cc-pwCVnZ-DK basis sets ($n=T, Q, \text{ and } 5$) [64]. The CBS limit was determined according to the methodology outlined in the ccECP paper for $3d$ TM elements [27]. Specifically, the Hartree-Fock (HF) energy was extrapolated using

$$E_n^{\text{HF}} = E_{\text{CBS}}^{\text{HF}} + a \exp[-bn]. \quad (23)$$

Similarly, the correlation energy, defined as the difference between CCSD(T) and HF energies, was extrapolated using

$$E_n^{\text{corr}} = E_{\text{CBS}}^{\text{corr}} + \frac{c}{(n+3/8)^3} + \frac{d}{(n+3/8)^5}. \quad (24)$$

To calculate binding curves and ΔE_i^{CC} in Eq. (21), we utilized the fully uncontracted aug-cc-pwCVQZ-DK basis sets [64].

For the OPH23 binding curve relative to the AE, the deviations from the CBS limit were found to be less than 7 meV, in the case of Co–O dimer. Previous research [27] has also suggested that the quadruple zeta level is adequate to calculate such binding curves. Deviations from the CBS limit in ΔE_i^{CC} were below 1.8 %, which is lower than the discrepancies observed between ccECP and AE excitation energies [41]. Data for the error estimations are provided in the Supporting Information.

IV. RESULTS AND DISCUSSION

A. Screening of PHs

In this Subsection, we discuss (1) how we selected the optimal HFOPT(X_{opt}) from HFOPT(X) ($X=2-6$) and (2) how we determined whether to employ HFOPT(X_{opt}) or CCOPT(X_{opt}) as the OPH23. As a reminder for the discussion below, PH names post-fixed with (X) denote potentials that were constructed to reproduce the energy spectrum with neutral excitation and ionization up to $+X$ charge in $3d$ and $4s$ levels.

The comparisons of the PHs are shown in Figure 2 for each element from Cr to Co, and in Figure 3 for each element from Ni to Zn. The vertical dashed and dotted lines in the left column indicate respectively the AE binding distance given by AE calculations and TM–O closest distance in the reference transition metal oxide listed in Table II. Accurate binding observed in this range is suitable to qualify a particular PH for use in target solid-state applications. The AE binding distances were obtained by the cubic spline interpolation.

Chromium: Every HFOPT reproduces the AE binding curve given by CCSD(T) within the chemical accuracy. HFOPT(4), HFOPT(5), and HFOPT(6) similarly give the lowest deviations. We made the CCOPT for $X=4$. Although CCOPT(4) does not reproduce the AE binding curve within the chemical accuracy in the very short distances unlike HFOPT(4), CCOPT(4) much better reproduces the excitation energy ($4s^1 3d^5 \rightarrow 4s^2 3d^4$) than HFOPT(4). We selected CCOPT(4) as the OPH23.

Manganese: Every HFOPT similarly reproduces the AE binding curve almost within the chemical accuracy. HFOPT(5) gives the smallest deviations around the AE binding distance so we made the CCOPT for $X=5$. CCOPT(5) gives larger deviations for the binding curve than HFOPT(5). We selected HFOPT(5) as the OPH23.

Iron: The HFOPTs give different binding curves. HFOPT(5) gives the smallest deviations among the HFOPTs. However, the chemical accuracy is not satisfied for the shorter distances. We made the CCOPT for $X=5$. CCOPT(5) reproduces the AE binding curve within the chemical accuracy and better reproduces the AE energy spectrum compared with HFOPT(5). We selected CCOPT(5) as the OPH23.

Cobalt: The HFOPTs give similar binding curves and do not satisfy the chemical accuracy for the shorter distances.

CCOPT(3) gives the smallest errors for the shorter distances. We made the CCOPT for $X=3$. CCOPT(3) reproduces the AE binding curve within the chemical accuracy and better reproduces the AE energy spectrum compared with HF OPT(3). We selected CCOPT(3) as the OPH23.

Nickel: Every HF OPT similarly reproduces the AE binding curve within the chemical accuracy. We made the CCOPT for $X=5$. CCOPT(5) does not reproduce the AE binding curve within the chemical accuracy for the shorter distances and give larger error for the excitation from $4s^1 3d^9 \rightarrow 4s^2 3d^8$. We selected HF OPT(5) as the OPH23. The remarkably large percentage error for the excitation is due to the very low excitation energy (~ 20 meV). Thus, 10 % error actually corresponds to only 2 meV.

Copper: HF OPT(2) (outside of the display range) and HF OPT(3) gave very large deviations for the binding curve. HF OPT(4), HF OPT(5), and HF OPT(6) reproduces the AE binding curve within chemical accuracy for the longer distances than the Cu–O closest distance in CuO solid. HF OPT(4) gives the lowest error within the HF OPTs so we made the CCOPT for $X=4$. However, CCOPT(4) does not reproduce the AE binding curve. We selected HF OPT(4) as the OPH23.

Zinc: The HF OPTs give very different binding curves depending on X . Among them, HF OPT(3) gives constant deviations from the AE binding curve (i.e., good reproducibility of curvature), so we choose the CCOPT for $X=3$. CCOPT(3) shows slightly smaller deviations for the binding curve and excellent reproducibility of the AE energy spectrum. We selected CCOPT(3) as the OPH23.

Note, with the exception of Mn, the other PHs are within chemical accuracy for the typical oxide’s distances listed in Table II. In contrast, the accuracy of the OPH23 set tends to decrease for shorter distances.

In summary, we selected CCOPT(X_{opt}) as the OPH23 for Cr, Fe, Co, and Zn and HF OPT(X_{opt}) for Mn, Ni, and Cu.

TABLE II. The TM–O and TM–F closest distances (Å) in transition metal oxides and fluorides.

TM–O name	TM–O distance	TM–F name	TM–F distance
Cr ₂ O ₃	2.012 [65]	CrF ₂	1.978 [66]
MnO	2.222 [67]	MnF ₂	2.128 [68]
FeO	2.154 [69]	FeF ₂	2.118 [70]
CoO	2.132 [71]	CoF ₂	2.058 [72]
NiO	2.072 [73]	NiF ₂	2.011 [72]
CuO	1.936 [74]	CuF ₂	1.917 [75]
ZnO	1.974 [76]	ZnF ₂	2.041 [77]

B. Validations and comparisons with state-of-the-art semilocal pseudopotentials

In the previous Subsection IV A, we chose a set of PHs OPH23 to be the ones that best reproduce the AE TM–O binding curves and AE ionization energies for each element. In

this Subsection, to test the transferability of OPH23, we investigate their ability to reproduce the AE TM–F binding curve.

The TM–O and TM–F binding curves obtained by our OPH23 and semilocal pseudopotentials, ccECP [27, 28], SBKJC [48, 49], and BFD [46, 47] relative to the AE results are shown in Figure 4 for Cr–Co and Figure 5 for Ni–Zn. The vertical dashed and dotted lines indicate the AE binding distance and TM–O/F closest distance in the reference oxide and fluoride listed in Table II.

For Mn–F case, we used ccECP binding curve as the reference instead of AE’s due to a convergence issue with the AE calculations. For these cases, the binding distance is also taken from the ccECP binding curve. Figure 4 shows that ccECP reproduces the AE binding curves very well for the other elements, so ccECP can be reasonably used as the reference.

Chromium: OPH23 reproduces the AE Cr–O binding curve within chemical accuracy whereas SBKJC and BFD do not satisfy the chemical accuracy. For Cr–F binding curve, OPH23 gives ~ 1.5 larger deviation than the chemical accuracy at the binding distance. The deviation gets smaller for longer distances. The deviations at the shorter distances are smaller than the typical magnitude of locality errors, 0.2–0.3 eV [25, 26].

Manganese: OPH23 reproduces the AE Mn–O binding curve almost within the chemical accuracy and reproduces the ccECP Mn–F binding curve within the chemical accuracy for distances longer than 1.5 Å.

Iron: OPH23 reproduces the AE Fe–O and Fe–F binding curves within the chemical accuracy. On the other hand, SBKJC (BFD) does not satisfy the chemical accuracy for Fe–O (Fe–F) binding curve, respectively.

Cobalt: OPH23 reproduces the AE Co–O and Co–F binding curves within the chemical accuracy. BFD gives significantly larger deviations for both Co–O and Co–F binding curves. This is also found for Ni, Cu, and Zn.

Nickel: OPH23 reproduces the AE Ni–O binding curve within the chemical accuracy. OPH23 gives slightly larger deviations for the Ni–F binding curve but they are significantly smaller than the typical magnitude of locality errors, 0.2–0.3 eV [25, 26].

Copper: OPH23 gives at most 0.1 eV deviation for the binding curves. Nevertheless, the deviations are significantly smaller than the typical magnitude of locality errors, 0.2–0.3 eV [25, 26].

Zinc: OPH23 reproduces the AE Zn–O and Zn–F binding curves almost within the chemical accuracy.

In summary, OPH23s reproduce the TM–O and TM–F binding curves within or close to chemical accuracy. Even when the deviations do exceed chemical accuracy, they are significantly smaller than the typical magnitude of locality errors, 0.2–0.3 eV [25, 26]. TM–F binding curve is never used to select the OPH23s. Therefore, the adequate reproducibil-

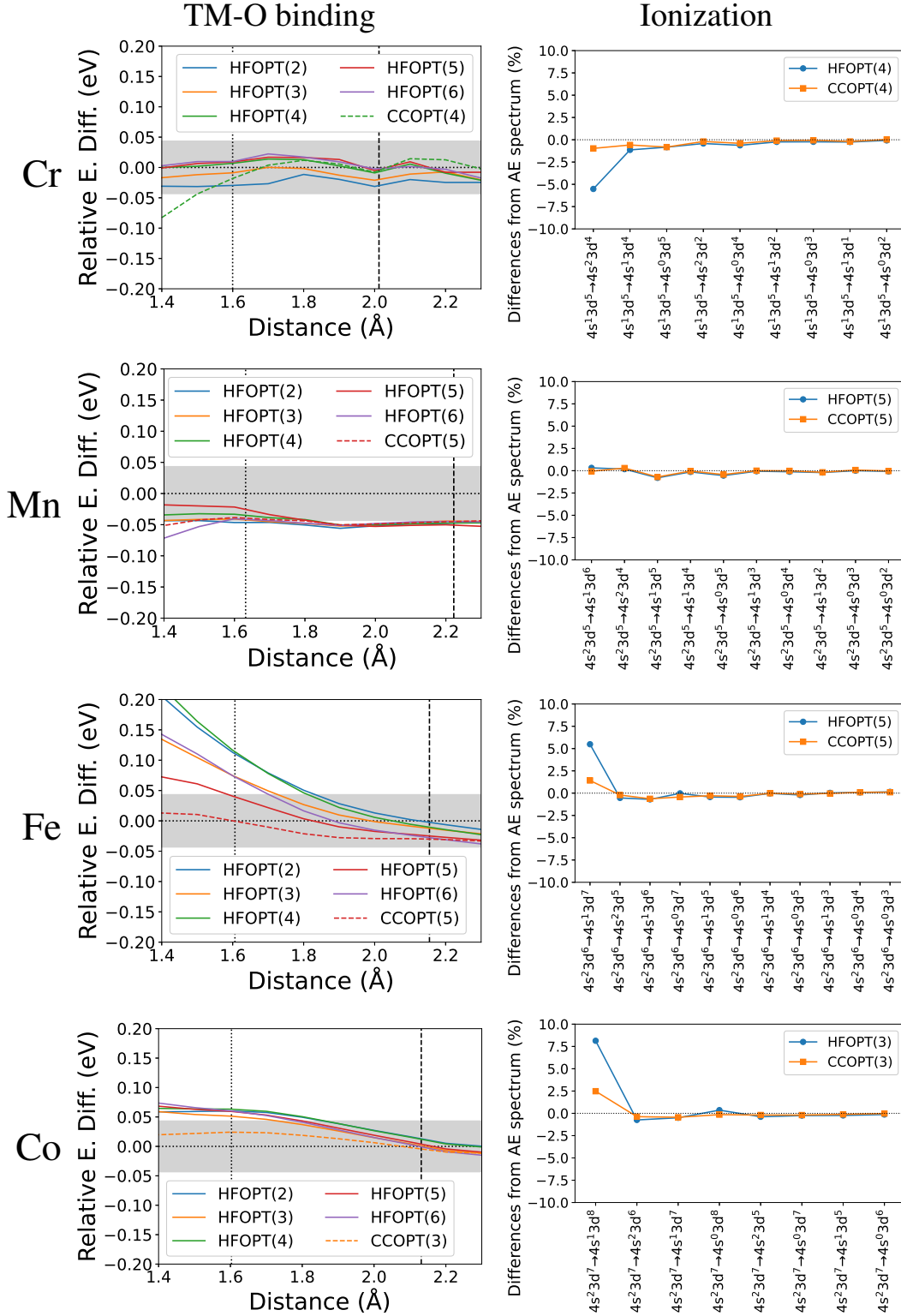


FIG. 2. (left) Absolute errors of TM-O binding curves (TM=Cr-Co) calculated via CCSD(T) for HFOPTs and CCOPT relative to the AE results. The vertical dashed and dotted lines indicate the AE binding distance and TM-O closest distance in the reference transition metal oxide listed in Table II. (right) Relative errors of the energy spectrum calculated with the best HFOPT and CCOPT relative to the AE results.

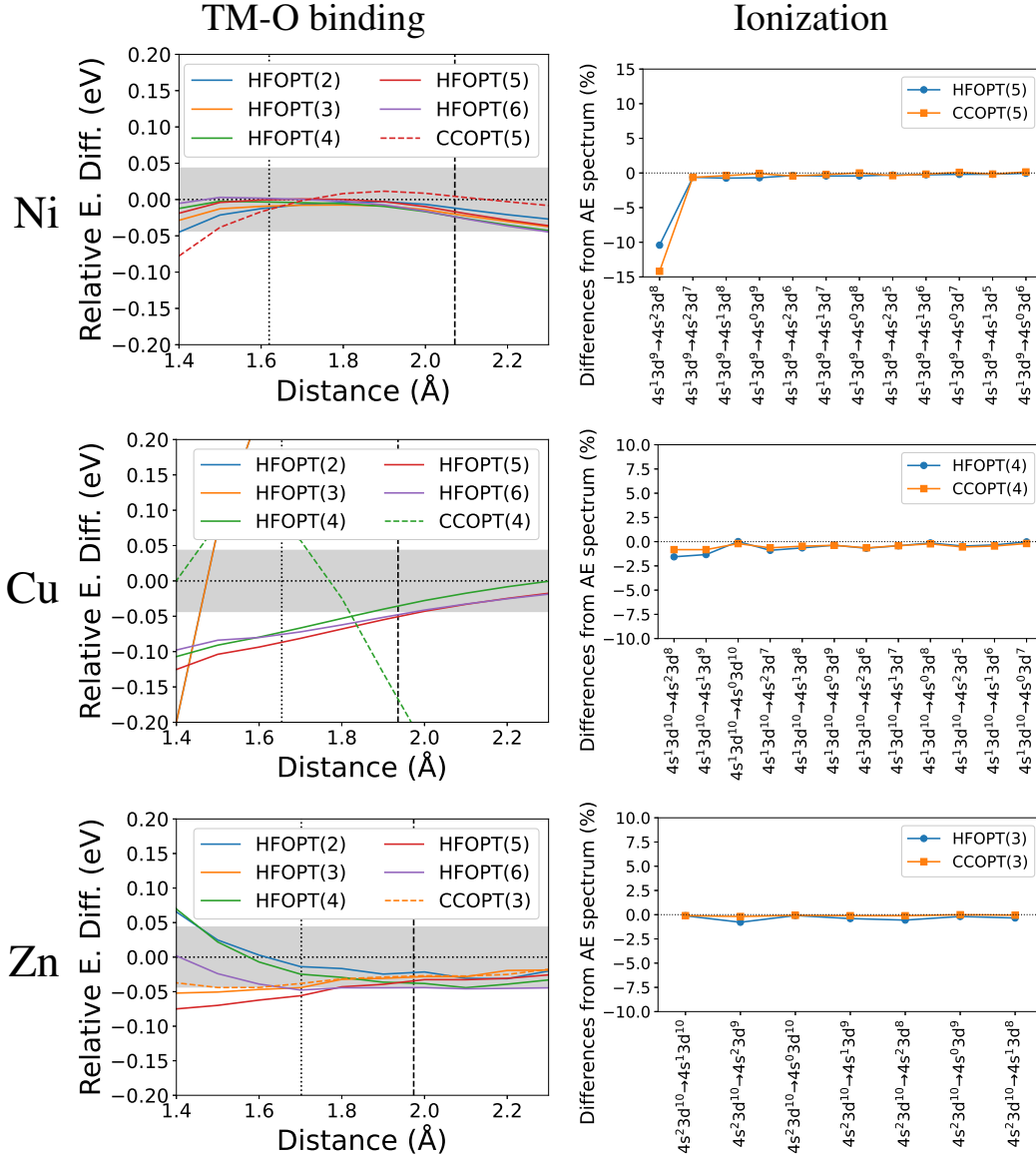


FIG. 3. (left) Absolute errors of TM-O binding curves (TM=Ni-Zn) calculated via CCSD(T) for HFOPTs and CCOPT relative to the AE results. The vertical dashed and dotted lines indicate the AE binding distance and TM-O closest distance in the reference transition metal oxide listed in Table II. (right) Relative errors of the energy spectrum calculated with the best HFOPT and CCOPT relative to the AE results.

ity of the AE TM-F binding curve provides assurances on the transferability of the OPH23s.

V. CONCLUSION

We have developed a set of PHs (OPH23) for the Cr–Zn transition metal elements. We have used a revised procedure from our previous work[41]. This procedure can be used for other elements in the periodic table. The set OPH23s are trained to reproduce all the valence orbital norms and eigenenergies with the HF method as well as the neutral excitation and ionization energy spectrum in $3d$ and $4s$ levels with the HF or CCSD(T) method using accurate semilocal pseudopotentials, and the AE TM–O binding curve with the CCSD(T) method. The set OPH23s reproduced the AE binding curves of TM–F within or quite near chemical accuracy. The largest deviation from the AE binding curve at the equilibrium distance was 0.067 eV of Cr–F. The accuracy of the PHs is comparable to the best FNDMC pseudopotentials in the literature [27, 28, 48, 49]. The pseudo-Hamiltonian approach removes the need of locality approximations in FNDMC, thus removing locality errors. Therefore, even when in some cases the deviations exceed chemical accuracy, they are significantly smaller than the typical magnitude of locality errors for transition metal elements, 0.2–0.3 eV [25, 26].

Our aim is, in the future, to employ the use of OPH23s to delve into an in-depth examination of strongly correlated transition metal complexes, focusing on their magnetic structures and other intrinsic properties. While the PHs were designed to reproduce the AE ionization energies and AE TM–O binding curves, they are found to reproduce the AE TM–F binding curves. Further test in solids are required to assess their transferability. This will be and addressed in future works.

SUPPORTING INFORMATION

We include the following data as supplementary materials: (1) The OPH23 set in XML format compatible with QMC-PACK, (2) Truncated form of the OPH23 set in the compatible formats with Molpro, Gaussian, and GAMESS, (3) Input and output files of calculations for the binding curves and ionization energies, and (4) A PDF file discussing the basis set errors relative to the CBS limit.

DATA AVAILABILITY STATEMENT

The data presented in this study are openly available as the supplementary materials.

ACKNOWLEDGMENTS

The work in ORNL (TI, CB, JK and FR) was supported by the U.S. Department of Energy, Office of Science, Ba-

sic Energy Sciences, Materials Sciences and Engineering Division. K.H. is grateful for financial support from MEXT-KAKENHI, Japan (JP19K05029, JP21K03400, JP22H02170, and JP23H04623), and the Air Force Office of Scientific Research, United States (Award Numbers: FA2386-22-1-4065). R.M. is grateful for financial supports from MEXT-KAKENHI (JP22H05146, JP21K03400 and JP19H04692), from the Air Force Office of Scientific Research (AFOSR-AOARD/FA2386-17-1-4049;FA2386-19-1-4015), and from JSPS Bilateral Joint Projects (JPJSBP120197714). An award of computer time was provided by the Innovative and Novel Computational Impact on Theory and Experiment (INCITE) program. This research used computational resources of the Oak Ridge Leadership Computing Facility, which is a DOE Office of Science User Facility supported under Contract DE-AC05-00OR22725. This research also used resources of the Research Center for Advanced Computing Infrastructure (RCACI) at JAIST.

APPENDIX

A. Angular momentum eigenfunctions

In the position representation with the spherical coordinates (r, θ, ϕ) , the eigenfunctions for the angular momentum eigenstates $|\ell m\rangle$ are given by the scalar spherical harmonics:

$$Y_{\ell}^m(\theta, \phi) = (-1)^{(m+|m|)/2} \sqrt{\frac{2\ell+1}{4\pi} \frac{(\ell-|m|)!}{(\ell+|m|)!}} P_{\ell}^{|m|}(\cos\theta) e^{im\phi}. \quad (25)$$

Here, $P_{\ell}^{|m|}(t)$ is the associated Legendre polynomials:

$$P_{\ell}^m(t) = \frac{1}{2^{\ell}} (1-t^2)^{\frac{m}{2}} \sum_{j=0}^{[(\ell-m)/2]} \frac{(-1)^j (2\ell-2j)!}{j! (\ell-j)! (\ell-2j-m)!} t^{\ell-2j-m}. \quad (26)$$

Here, $[(\ell-m)/2]$ indicates the maximum integer less than or equal to $(\ell-m)/2$.

B. Justification of the many-body correction

The difference of excitation energies between HF and CCSD(T) almost does not depend on the choice of ECP [27, 41] so

$$\left(\Delta E_i^{\text{CCSD(T),CCOPT}} - \Delta E_i^{\text{HF,CCOPT}} \right) \approx \left(\Delta E_i^{\text{CCSD(T),HF OPT}} - \Delta E_i^{\text{HF,HF OPT}} \right). \quad (27)$$

Thus, the numerator in the parentheses of (21) is approximated as

$$\Delta E_i^{\text{CCSD(T),CCOPT}} - \Delta E_i^{\text{CCSD(T),ccECP}}. \quad (28)$$

Therefore, the minimization of the cost function in Eq. (21) corresponds to the optimization so as to reproduce the electron excitation energies at the CCSD(T) level.

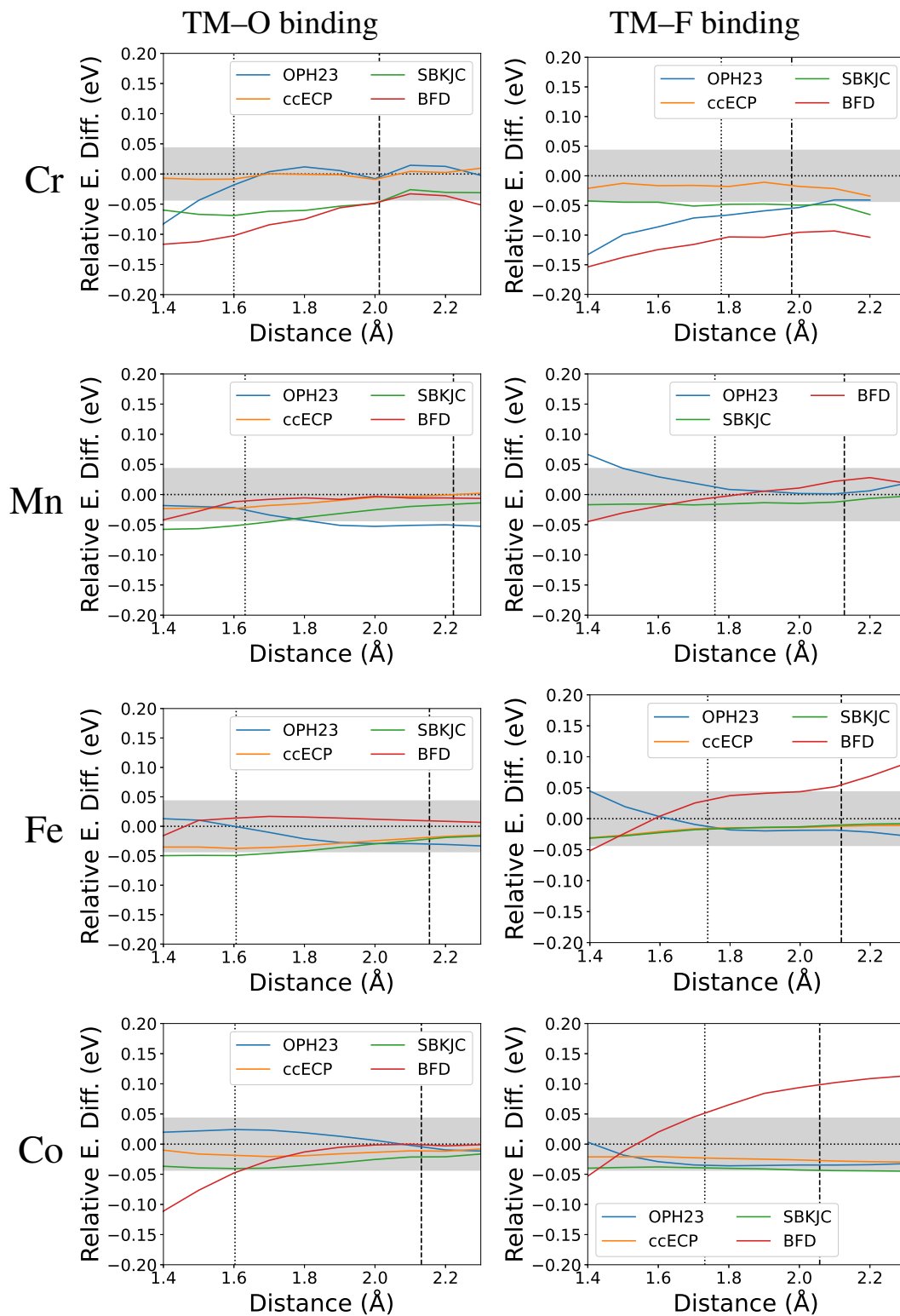


FIG. 4. Binding curves of TM-O and TM-F molecules (TM=Cr-Co) for OPH23 and select community ECPs relative to the AE CCSD(T) results. For the Mn-F case, the binding curves are drawn relative to the ccECP results, because the AE calculations do not converge. The vertical dashed and dotted lines indicate the AE binding distance (ccECP is used for the Mn-F case) and TM-O(F) closest distance in the reference transition metal oxide (fluoride) listed in Table II.

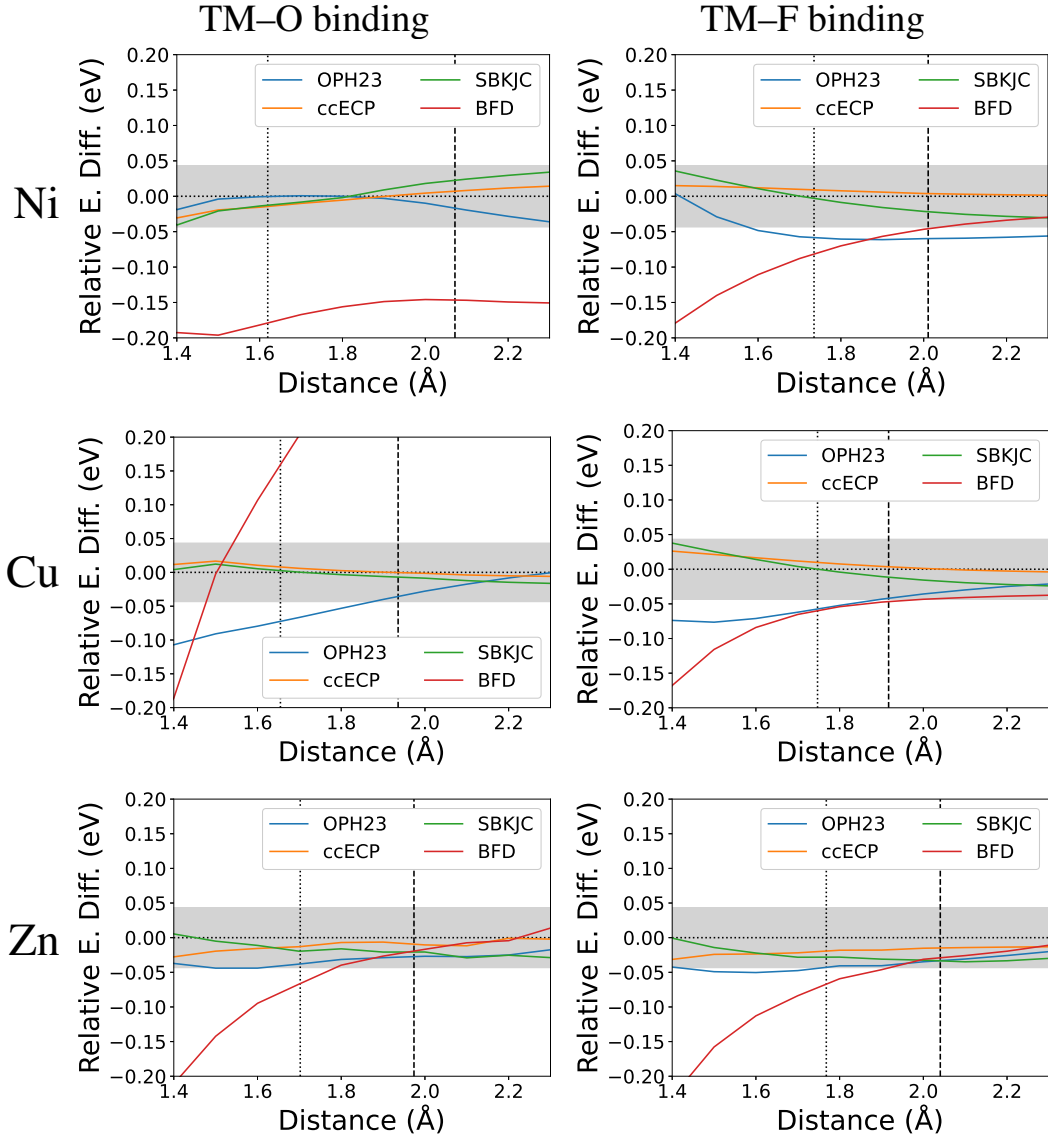


FIG. 5. Binding curves of TM–O and TM–F molecules (TM=Ni–Zn) for OPH23 and select community ECPs relative to the AE CCSD(T) results. The vertical dashed and dotted lines indicate the AE binding distance given by AE calculations and TM–O(F) closest distance in the reference transition metal oxide (fluoride) listed in Table II.

-
- [1] T. Ichibha, Y. Zhang, K. Hongo, R. Maezono, and F. A. Reboredo, Candidate structure for the H₂-PRE phase of solid hydrogen, *Phys. Rev. B* **104**, 214111 (2021).
- [2] K. Oka, T. Ichibha, D. Kato, Y. Noda, Y. Tominaga, K. Yamada, M. Iwasaki, N. Noma, K. Hongo, R. Maezono, and F. A. Reboredo, Anionic ordering in Pb₂Ti₄O₉F₂ revisited by nuclear magnetic resonance and density functional theory, *Dalton Trans.* **51**, 15361 (2022).
- [3] A. Jain, S. P. Ong, G. Hautier, W. Chen, W. D. Richards, S. Dacek, S. Cholia, D. Gunter, D. Skinner, G. Ceder, and K. A. Persson, Commentary: The Materials Project: A materials genome approach to accelerating materials innovation, *APL Mater.* **1** (2013).
- [4] W. M. Foulkes, L. Mitas, R. J. Needs, and G. Rajagopal, Quantum Monte Carlo simulations of solids, *Rev. Mod. Phys.* **73**, 33 (2001).
- [5] Y. Luo, P. W. Doak, and P. R. C. Kent, A High-Performance Design for Hierarchical Parallelism in the QMCPACK Monte Carlo code (2022) pp. 22–27.
- [6] M. J. Gillan, F. R. Manby, M. D. Towler, and D. Alfè, Assessing the accuracy of quantum Monte Carlo and density functional theory for energetics of small water clusters, *J. Chem. Phys.* **136**, 244105 (2012).
- [7] B. Brito, L. Cândido, J. T. Rabelo, and G.-Q. Hai, Binding energies of small lithium clusters: A comparison of different theoretical calculations, *Chem. Phys. Lett.* **616-617**, 212 (2014).

- [8] M. Dubecký, P. Jurečka, R. Derian, P. Hobza, M. Otyepka, and L. Mitas, Quantum Monte Carlo Methods Describe Noncovalent Interactions with Subchemical Accuracy, *J. Chem. Theory Comput.* **9**, 4287 (2013), pMID: 26589147.
- [9] R. Grimm and R. Storer, Monte-Carlo solution of Schrödinger's equation, *J. Comput. Phys.* **7**, 134 (1971).
- [10] J. B. Anderson, Quantum chemistry by random walk. H^2P , H_3^+ , $D_{3h}^{-1}A_1'$, $H_2^+ 3\Sigma_u^+$, $H_4^+ 1\Sigma_g^+$, Be^1S , *J. Chem. Phys.* **65**, 4121 (1976).
- [11] W. Kohn and L. J. Sham, Self-Consistent Equations Including Exchange and Correlation Effects, *Phys. Rev.* **140**, A1133 (1965).
- [12] M. A. Morales, J. McMinis, B. K. Clark, J. Kim, and G. E. Scuseria, Multideterminant Wave Functions in Quantum Monte Carlo, *J. Chem. Theory Comput.* **8**, 2181 (2012).
- [13] A. Benali, K. Gasperich, K. D. Jordan, T. Applencourt, Y. Luo, M. C. Bennett, J. T. Krogel, L. Shulenburger, P. R. C. Kent, P.-F. Loos, A. Scemama, and M. Caffarel, Toward a systematic improvement of the fixed-node approximation in diffusion Monte Carlo for solids—A case study in diamond, *J. Chem. Phys.* **153**, 184111 (2020).
- [14] P. López Ríos, A. Ma, N. D. Drummond, M. D. Towler, and R. J. Needs, Inhomogeneous backflow transformations in quantum monte carlo calculations, *Phys. Rev. E* **74**, 066701 (2006).
- [15] R. Maezono, P. López Ríos, T. Ogawa, and R. J. Needs, Excitons and biexcitons in symmetric electron-hole bilayers, *Phys. Rev. Lett.* **110**, 216407 (2013).
- [16] R. Maezono, N. D. Drummond, A. Ma, and R. J. Needs, Diamond to β -tin phase transition in si within diffusion quantum monte carlo, *Phys. Rev. B* **82**, 184108 (2010).
- [17] D. M. Ceperley, The statistical error of green's function Monte Carlo, *J. Stat. Phys.* **43**, 815 (1986).
- [18] B. L. Hammond, P. J. Reynolds, and W. A. Lester, Valence quantum Monte Carlo with ab initio effective core potentials, *J. Chem. Phys.* **87**, 1130 (1987).
- [19] B. L. Hammond, P. J. Reynolds, and W. A. Lester, Damped-Core Quantum Monte Carlo Method: Effective Treatment for Large-Z Systems, *Phys. Rev. Lett.* **61**, 2312 (1988).
- [20] J. Koseki, R. Maezono, M. Tachikawa, M. D. Towler, and R. J. Needs, Quantum Monte Carlo study of porphyrin transition metal complexes, *The Journal of Chemical Physics* **129**, 085103 (2008), https://pubs.aip.org/aip/jcp/article-pdf/doi/10.1063/1.2966003/15418830/085103_1_online.pdf.
- [21] L. Mitáš, E. L. Shirley, and D. M. Ceperley, Nonlocal pseudopotentials and diffusion Monte Carlo, *J. Chem. Phys.* **95**, 3467 (1991).
- [22] M. Casula, Beyond the locality approximation in the standard diffusion Monte Carlo method, *Phys. Rev. B* **74**, 161102 (2006).
- [23] L. Mitáš, E. L. Shirley, and D. M. Ceperley, Nonlocal pseudopotentials and diffusion Monte Carlo, *J. Chem. Phys.* **95**, 3467 (1991).
- [24] J. T. Krogel and F. A. Reboredo, Hybridizing pseudo-Hamiltonians and non-local pseudopotentials in diffusion Monte Carlo, *J. Chem. Phys.* **153**, 104111 (2020).
- [25] J. Yu, L. K. Wagner, and E. Ertekin, Towards a systematic assessment of errors in diffusion Monte Carlo calculations of semiconductors: Case study of zinc selenide and zinc oxide, *J. Chem. Phys.* **143**, 224707 (2015).
- [26] J. A. Santana, J. T. Krogel, J. Kim, P. R. C. Kent, and F. A. Reboredo, Structural stability and defect energetics of ZnO from diffusion quantum Monte Carlo, *J. Chem. Phys.* **142**, 164705 (2015).
- [27] A. Annaberdiyev, G. Wang, C. A. Melton, M. C. Bennett, L. Shulenburger, and L. Mitas, A new generation of effective core potentials from correlated calculations: 3d transition metal series, *Journal = J. Chem. Phys.*, volume = 149, number = 13, pages = 134108, year = 2018, doi = 10.1063/1.5040472, url = <https://doi.org/10.1063/1.5040472>, .
- [28] M. C. Bennett, C. A. Melton, A. Annaberdiyev, G. Wang, L. Shulenburger, and L. Mitas, A new generation of effective core potentials for correlated calculations, *J. Chem. Phys.* **147**, 224106 (2017).
- [29] R. Nazarov, L. Shulenburger, M. Morales, and R. Q. Hood, Benchmarking the pseudopotential and fixed-node approximations in diffusion Monte Carlo calculations of molecules and solids, *Phys. Rev. B* **93**, 094111 (2016).
- [30] J. T. Krogel and P. R. Kent, Magnitude of pseudopotential localization errors in fixed node diffusion quantum Monte Carlo, *J. Chem. Phys.* **146**, 244101 (2017).
- [31] A. L. Dzubak, J. T. Krogel, and F. A. Reboredo, Quantitative estimation of localization errors of 3 d transition metal pseudopotentials in diffusion Monte Carlo, *J. Chem. Phys.* **147**, 024102 (2017).
- [32] C. J. Umrigar, J. Toulouse, C. Filippi, S. Sorella, and R. G. Hennig, Alleviation of the Fermion-Sign Problem by Optimization of Many-Body Wave Functions, *Phys. Rev. Lett.* **98**, 110201 (2007).
- [33] S. Zhang and H. Krakauer, Quantum Monte Carlo Method using Phase-Free Random Walks with Slater Determinants, *Phys. Rev. Lett.* **90**, 136401 (2003).
- [34] W. Al-Saidi, S. Zhang, and H. Krakauer, Auxiliary-field quantum Monte Carlo calculations of molecular systems with a Gaussian basis, *J. Chem. Phys.* **124**, 224101 (2006).
- [35] M. Suewattana, W. Purwanto, S. Zhang, H. Krakauer, and E. J. Walter, Phaseless auxiliary-field quantum Monte Carlo calculations with plane waves and pseudopotentials: Applications to atoms and molecules, *Phys. Rev. B* **75**, 245123 (2007).
- [36] E. Pavarini, E. Koch, and U. Schollwöck, eds., *Emergent Phenomena in Correlated Matter*, Schriften des Forschungszentrums Jülich. Reihe modeling and simulation, Vol. 3 (Forschungszentrum Jülich GmbH Zentralbibliothek, Verlag, Jülich, 2013) p. 520 S.
- [37] G. B. Bachelet, D. M. Ceperley, and M. G. B. Chiochetti, Novel pseudo-Hamiltonian for quantum Monte Carlo simulations, *Phys. Rev. Lett.* **62**, 2088 (1989).
- [38] W. M. C. Foulkes and M. Schluter, Pseudopotentials with position-dependent electron masses, *Phys. Rev. B* **42**, 11505 (1990).
- [39] X.-P. Li, D. M. Ceperley, and R. M. Martin, Cohesive energy of silicon by the green's-function monte carlo method, *Phys. Rev. B* **44**, 10929 (1991).
- [40] A. Bosin, V. Fiorentini, A. Lastrì, and G. B. Bachelet, Pseudohamiltonians and quantum monte carlo, *MRS Online Proceedings Library (OPL)* **291**, 21 (1992).
- [41] M. C. Bennett, F. A. Reboredo, L. Mitas, and J. T. Krogel, High Accuracy Transition Metal Effective Cores for the Many-Body Diffusion Monte Carlo Method, *J. Chem. Theory Comput.* **18**, 828 (2022).
- [42] M. Bajdich, L. Mitas, G. Drobný, L. K. Wagner, and K. E. Schmidt, Pfaffian Pairing Wave Functions in Electronic-Structure Quantum Monte Carlo Simulations, *Phys. Rev. Lett.* **96**, 130201 (2006).
- [43] M. Bajdich, L. Mitas, L. K. Wagner, and K. E. Schmidt, Pfaffian pairing and backflow wavefunctions for electronic structure quantum Monte Carlo methods, *Phys. Rev. B* **77**, 115112 (2008).
- [44] C. Genovese, T. Shirakawa, K. Nakano, and S. Sorella, General Correlated Geminal Ansatz for Electronic Structure Calculations: Exploiting Pfaffians in Place of Determinants, *J. Chem.*

- Theory Comput. **16**, 6114 (2020).
- [45] M. C. Bennett, F. A. Reboredo, L. Mitas, and J. T. Krogel, High Accuracy Transition Metal Effective Cores for the Many-Body Diffusion Monte Carlo Method, *J. Chem. Theory Comput.* **18**, 828 (2022).
- [46] M. Burkatzki, C. Filippi, and M. Dolg, Energy-consistent pseudopotentials for quantum Monte Carlo calculations, *J. Chem. Phys.* **126**, 234105 (2007).
- [47] M. Burkatzki, C. Filippi, and M. Dolg, Energy-consistent small-core pseudopotentials for 3d-transition metals adapted to quantum Monte Carlo calculations, *J. Chem. Phys.* **129**, 164115 (2008).
- [48] W. J. Stevens, H. Basch, and M. Krauss, Compact effective potentials and efficient shared-exponent basis sets for the first- and second-row atoms, *J. Chem. Phys.* **81**, 6026 (1984).
- [49] W. J. Stevens, M. Krauss, H. Basch, and P. G. Jasien, Relativistic compact effective potentials and efficient, shared-exponent basis sets for the third-, fourth-, and fifth-row atoms, *Can. J. Chem.* **70**, 612 (1992).
- [50] M. Dolg, U. Wedig, H. Stoll, and H. Preuss, Energy-adjusted ab initio pseudopotentials for the first row transition elements, *The Journal of Chemical Physics* **86**, 866 (1987), https://pubs.aip.org/aip/jcp/article-pdf/86/2/866/11058005/866.1_online.pdf.
- [51] D. M. Ceperley and L. Mitas, Quantum monte carlo methods in chemistry, in *Advances in Chemical Physics* (John Wiley & Sons, Ltd, 1996) pp. 1–38, <https://onlinelibrary.wiley.com/doi/pdf/10.1002/9780470141526.ch1>.
- [52] L. Mitas, Quantum monte carlo calculation of the fe atom, *Phys. Rev. A* **49**, 4411 (1994).
- [53] G. Wang, A. Annaberdiev, C. A. Melton, M. C. Bennett, L. Shulenburger, and L. Mitas, A new generation of effective core potentials from correlated calculations: 4s and 4p main group elements and first row additions, *J. Chem. Phys.* **151**, 144110 (2019), <https://doi.org/10.1063/1.5121006>.
- [54] J. T. Krogel, Nexus: A modular workflow management system for quantum simulation codes, *Comput. Phys. Commun.* **198**, 154 (2016).
- [55] J. A. Nelder and R. Mead, A Simplex Method for Function Minimization, *Comput. J.* **7**, 308 (1965).
- [56] W. Spendley, G. R. Hext, and F. R. Himsworth, Sequential Application of Simplex Designs in Optimisation and Evolutionary Operation, *Technometrics* **4**, 441 (1962).
- [57] P. Virtanen, R. Gommers, T. E. Oliphant, M. Haberland, T. Reddy, D. Cournapeau, E. Burovski, P. Peterson, W. Weckesser, J. Bright, S. J. van der Walt, M. Brett, J. Wilson, K. J. Millman, N. Mayorov, A. R. J. Nelson, E. Jones, R. Kern, E. Larson, C. J. Carey, Í. Polat, Y. Feng, E. W. Moore, J. VanderPlas, D. Laxalde, J. Perktold, R. Cimrman, I. Henriksen, E. A. Quintero, C. R. Harris, A. M. Archibald, A. H. Ribeiro, F. Pedregosa, P. van Mulbregt, and SciPy 1.0 Contributors, SciPy 1.0: Fundamental Algorithms for Scientific Computing in Python, *Nat. Methods* **17**, 261 (2020).
- [58] S. Kotochigova, Z. H. Levine, E. L. Shirley, M. D. Stiles, and C. W. Clark, Local-density-functional calculations of the energy of atoms, *Phys. Rev. A* **55**, 191 (1997).
- [59] S. Kotochigova, Z. H. Levine, E. L. Shirley, M. D. Stiles, and C. W. Clark, Erratum: Local-density-functional calculations of the energy of atoms [Phys. Rev. A 55, 191 (1997)], *Phys. Rev. A* **56**, 5191 (1997).
- [60] H.-J. Werner, P. J. Knowles, G. Knizia, F. R. Manby, and M. Schütz, Molpro: a general-purpose quantum chemistry program package, *Wiley Interdiscip. Rev.: Comput. Mol. Sci.* **2**, 242 (2011).
- [61] H.-J. Werner, P. J. Knowles, F. R. Manby, J. A. Black, K. Doll, A. Heßelmann, D. Kats, A. Köhn, T. Korona, D. A. Kreplin, Q. Ma, T. F. Miller, A. Mitrushchenkov, K. A. Peterson, I. Polyak, G. Rauhut, and M. Sibaev, The Molpro quantum chemistry package, *J. Chem. Phys.* **152**, 144107 (2020).
- [62] M. Douglas and N. M. Kroll, Quantum electrodynamic corrections to the fine structure of helium, *Ann. Phys.* **82**, 89 (1974).
- [63] B. A. Hess, Relativistic electronic-structure calculations employing a two-component no-pair formalism with external-field projection operators, *Phys. Rev. A* **33**, 3742 (1986).
- [64] N. B. Balabanov and K. A. Peterson, Basis set limit electronic excitation energies, ionization potentials, and electron affinities for the 3d transition metal atoms: Coupled cluster and multireference methods, *J. Chem. Phys.* **125**, 074110 (2006).
- [65] A. Kantor, I. Kantor, M. Merlini, K. Glazyrin, C. Prescher, M. Hanfland, and L. Dubrovinsky, High-pressure structural studies of eskolaite by means of single-crystal X-ray diffraction, *Am. Mineral.* **97**, 1764 (2012).
- [66] R. W. G. Wyckoff, *Crystal structures*, Second edition. Rutil structure, **1**, 239 (1963).
- [67] R. Pacalo and E. Graham, Pressure and temperature dependence of the elastic properties of synthetic mno, *Phys. Chem. Miner.* **18**, 69 (1991).
- [68] Y. T. Hazen, R.M. and L. Finger, Crystal structure and compressibility of MnF₂ to 15 kbar, *Year Book - Carnegie Inst. Washington* **77**, 841 (1978).
- [69] H. Fjellvåg, B. C. Hauback, T. Vogt, and S. Stølen, Monoclinic nearly stoichiometric wustite at low temperatures, *Am. Mineral.* **87**, 347 (2002).
- [70] W. H. Baur and A. A. Khan, Rutile-type compounds. IV. SiO₂, GeO₂ and a comparison with other rutile-type structures, *Acta Crystallogr., Sect. B: Struct. Crystallogr. Cryst. Chem.* **27**, 2133 (1971).
- [71] S. SASAKI, K. FUJINO, and Y. Takéuchi, X-Ray Determination of Electron-Density Distributions in Oxides, MgO, MnO, CoO, and NiO, and Atomic Scattering Factors of their Constituent Atoms, *Proceedings of the Japan Academy, Series B* **55**, 43 (1979).
- [72] M. M. Costa, J. Paixao, M. J. de Almeida, and L. C. Andrade, Charge densities of two rutile structures: NiF₂ and CoF₂, *Acta Crystallogr., Sect. B: Struct. Sci.;(Denmark)* **49** (1993).
- [73] H. Taguchi, Relationship between crystal structure and electrical properties of murdochite-type Ni_{6+2x}Mn_{1-x}O₈, *Solid State Commun.* **108**, 635 (1998).
- [74] N. Calos, J. Forrester, and G. Schaffer, A crystallographic contribution to the mechanism of a mechanically induced solid state reaction, *J. Solid State Chem.* **122**, 273 (1996).
- [75] P. Fischer, W. Hälg, D. Schwarzenbach, and H. Gamsjäger, Magnetic and crystal structure of copper (II) fluoride, *J. Phys. Chem. Solids* **35**, 1683 (1974).
- [76] K. Kihara and G. Donnay, Anharmonic thermal vibrations in ZnO, *Can. Mineral.* **23**, 647 (1985).
- [77] N. J. O’Toole and V. A. Streltsov, Synchrotron x-ray analysis of the electron density in CoF₂ and ZnF₂, *Acta Crystallogr., Sect. B: Struct. Sci.* **57**, 128 (2001).